International Journal of Greenhouse Gas Control 105 (2021) 103244

Contents lists available at ScienceDirect

International Journal of Greenhouse Gas Control

journal homepage: www.elsevier.com/locate/ijggc

Sediment acidification and temperature increase in an artificial CO_2 vent

Dirk de Beer [a,*], Anna Lichtschlag [b], Anita Flohr [b,c], Marit Rianne van Erk [a], Soeren Ahmerkamp [a], Moritz Holtappels [d], Matthias Haeckel [e], James Strong [b]

[a] Max-Planck-Institute for Marine Microbiology, Celciusstrasse 1, 28359, Bremen, Germany
[b] National Oceanography Centre, European Way, Southampton, SO14 3ZH, United Kingdom
[c] University of Southampton, Waterfront Campus, European Way, Southampton, SO14 3ZH, UK
[d] Alfred Wegener Institute for Polar and Marine Research, Am Handelshafen 12, 27570, Bremerhaven, Germany
[e] GEOMAR Helmholtz Centre for Ocean Research Kiel, Wischhofstr. 1-3, 24148, Kiel, Germany

ARTICLE INFO

Keywords:
CO_2 vents
Calcite dissolution
Silicate weathering
Vent modelling
In situ measurements

ABSTRACT

We investigated the effect of an artificial CO_2 vent (0.0015−0.037 mol s^{-1}), simulating a leak from a reservoir for carbon capture and storage (CCS), on the sediment geochemistry. CO_2 was injected 3 m deep into the seafloor at 120 m depth. With increasing mass flow an increasing number of vents were observed, distributed over an area of approximately 3 m. *In situ* profiling with microsensors for pH, T, O_2 and ORP showed the geochemical effects are localized in a small area around the vents and highly variable. In measurements remote from the vent, the pH reached a value of 7.6 at a depth of 0.06 m. In a CO_2 venting channel, pH reduced to below 5. Steep temperature profiles were indicative of a heat source inside the sediment. Elevated total alkalinity and Ca^{2+} levels showed calcite dissolution. Venting decreased sulfate reduction rates, but not aerobic respiration. A transport-reaction model confirmed that a large fraction of the injected CO_2 is transported laterally into the sediment and that the reactions between CO_2 and sediment generate enough heat to elevate the temperature significantly. A CO_2 leak will have only local consequences for sediment biogeochemistry, and only a small fraction of the escaped CO_2 will reach the sediment surface.

1. Introduction

CCS entails the capturing of CO_2 from large point sources such as industrial plants (steel mills, cement factories and power plants), and depositing it in an underground geological formation. CCS may be a future strategy to reduce CO_2 emissions and thereby combat the ensuing global climate change and ocean acidification. Although much more costly than storage on land, offshore storage of CO_2 in depleted oil and gas reservoirs and saline aquifers is politically the most acceptable. Currently several offshore CCS demonstration projects are operational (Petrobras Brazil, Sleipner Norway) and several more are being planned. For these demonstrations it is critical to be able to detect possible leaks from the reservoirs and assess the ecological effect of such leaks.

Volcanic vents have been studied to assess the effects of elevated CO_2 on biological diversity (Fabricius et al., 2011), physiology (de Beer et al., 2013; Hofmann et al., 2015), ecosystem functioning (Hall-Spencer et al., 2008; Russell et al., 2013) and geochemical processes (Fink et al., 2017; Molari et al., 2018). Such natural vents however, do not only contain CO_2, but a variety of other gasses like CH_4, H_2S and H_2 which complicate interpretation of data (Fink et al., 2017; Rizzo et al., 2019). Moreover, volcanic vents are of much larger scale than potential CO_2 leaks from CCS sites. The areas can encompass entire coastal zones or deep-sea mounts, and the CO_2 emission rates dwarf potential CCS leaks. Therefore, small scale experiments with pure CO_2 are needed (Dean et al., 2020; Vielstädte et al., 2019).

Methods that can be used to sense leaks can be aimed to detect gas bubbles or changes in the water column chemistry. Visual methods are unsuitable as visibility is limited and bubbles are hard to spot. Acoustics are extremely sensitive for detecting bubble streams (von Deimling et al., 2010), but are not quantitative and will not detect dissolved CO_2. Upon dissolution, CO_2 hydrates under generation of acidity:

$$CO_2 + H_2O \rightarrow H_2CO_3 \rightarrow HCO_3^- + H^+ \quad (1)$$

Thus dissolved CO_2 can be detected by the resulting pH decrease, or quantified with an eddy covariance method for dissolved inorganic carbon (DIC) (Long et al., 2015). The sediment biogeochemistry of

* Corresponding author.
E-mail address: dbeer@mpi-bremen.de (D. de Beer).

https://doi.org/10.1016/j.ijggc.2020.103244
Received 11 September 2020; Received in revised form 25 November 2020; Accepted 15 December 2020
Available online 31 December 2020
1750-5836/Crown Copyright © 2020 Published by Elsevier Ltd. This is an open access article under the CC BY-NC-ND license (http://creativecommons.org/licenses/by-nc-nd/4.0/).

Table 1
Overview of the CO_2 flow rates during the *in situ* experiment.

Mol s^{-1}	Kg day^{-1}	date	Time of day	Interval (h)	L CO_2 total	Moles CO_2 total
0.0015	5.7	10/5	20.00	91	10,920	488
0.0037	14.1	14/5	15.00	16	4800	214
0.0074	28.1	15/5	7.00	58	34,800	1554
0.022	83.6	17/5	17.00	47	84,600	3777
0.037	140.7	19/5	16.00	66	198,000	8839
0	0	22/5	12.00			

natural vents was investigated in several studies, but most of these were aimed to the effects of vents on biodiversity. CO_2 venting leads to acidification of the porewater and vented areas have a spatially heterogeneous biogeochemistry (de Beer et al., 2013; Molari et al., 2018; Rizzo et al., 2019). In and near natural shallow CO_2 vents biodiversity tends to decrease (Fabricius et al., 2011), seagrass growth is stimulated (Hall-Spencer et al., 2008), meiofauna becomes reduced (Guilini et al., 2017; Mevenkamp et al., 2018) and microbial communities decrease in density and diversity (Molari et al., 2018). As the organisms may well be adapted to high CO_2, it was remarked that natural laboratories have limited relevance for effects of sudden leaks from reservoirs on biology (Ziogou et al., 2013). Depth below sea level strongly enhances the acidification as due to the pressure much higher concentrations can be reached (Konno et al., 2006). Especially at depths where the hydrostatic pressure allows formation of liquid CO_2 limits to life become evident (de Beer et al., 2013).

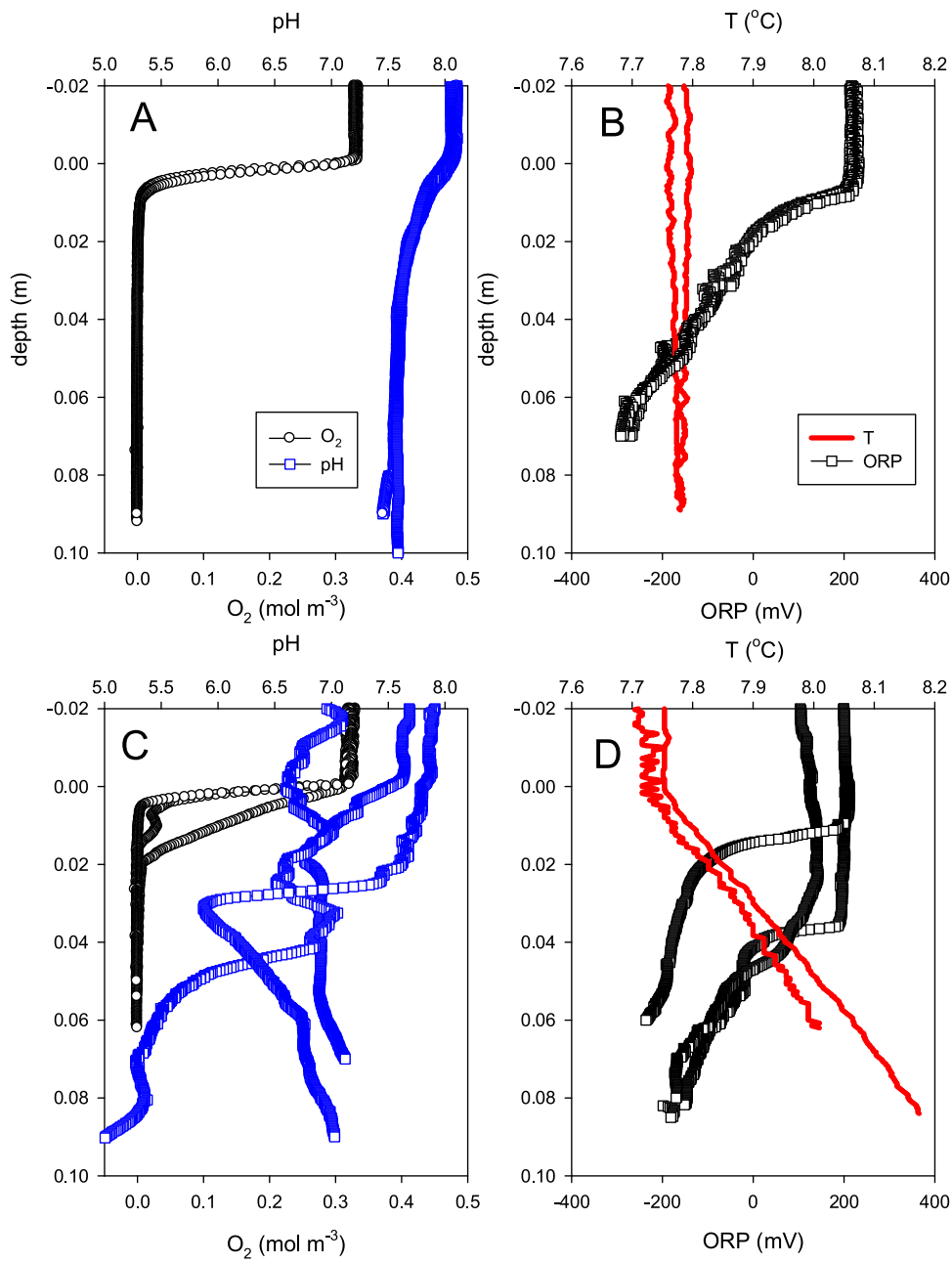

Fig. 1. Typical *in situ* profiles in the background (A,B) and in the vent (C, D). The background profiles were all very similar. The profiles measured in the vents were highly variable, especially the pH and oxidation-reduction potential (ORP). The typical effects of venting are a reduced pH and elevated temperature.

Much less is documented on the effects of porewater acidification on the sediment geochemistry. Obviously, the acidification will lead to calcite dissolution, and at higher CO_2 concentrations will eventually induce silicate weathering (Wallmann et al., 2008; Wan et al., 2017). Both processes will neutralize CO_2 by conversion to bicarbonate coupled to proton scavenging. Consequently, CO_2 concentrations can be decreased by such reactions during the passage to the sediment surface (Lichtschlag et al., 2015).

To study in detail the events at the seafloor upon a leak from a CO_2 storage, an artificial CO_2 vent was created in the North Sea, close to an abandoned gas platform above a depleted gas field that is considered suitable for CCS. The main aim of the project was to evaluate methods for detection and quantification of CO_2 leakage from a storage complex. We specifically aimed to assess effects on local geochemistry, the size of the vent area, and microbial degradation rates.

2. Methods

2.1. CO_2 injection in the seabottom

The field experiment and measurements were conducted during expedition JC180 with the royal research vessel James Cook in April-May 2019. A complete description of the engineering was given in a separate paper (Flohr et al., 2020). In short, a curved injection pipe of 5 m long was brought in the seafloor, with the opening at 3 m below the seafloor. A tank containing liquid CO_2 was placed on the seafloor at 100 m distance and connected to the injection pipe (Flohr et al., 2020). CO_2 flow started on May 10, 2019, and was stepwise increased from 0.0015 to 0.037 mol s^{-1} (Table 1). The experiment was terminated on May 22, 2019. The experiment is illustrated by underwater photos in Fig. 1 of the Supplement.

2.2. Microsensor measurements

Using an autonomous deep sea profiler, microprofiles were measured in the sediments along 4–20 m long transects, where the profiler was moved in steps along a line from the outside of the area towards the vent area. The *in situ* deep-sea microsensor profiler as described previously (Glud et al., 2013) was equipped with 3 microsensors for O_2, 2 for H_2S, 3 for pH, 2 for ORP (oxidation-reduction potential) and 1 for temperature. The pH sensors were glass electrodes in a steel needle (MI414, Microelectrodes, Bedford USA), for which an external reference was used. The other sensors were made and calibrated as described previously (de Beer et al., 2013; Fink et al., 2017). The profiler was preprogrammed for profiles over a depth of 12 cm, starting a few cm above the seafloor. The profiler was brought to the seafloor by a Remotely Operate Vehicle (ROV, named ISIS) that could start the profiling program using a magnetic starter (Suppl. Fig. 1). After each profile measurement, which took 1 h, the profiler was repositioned and restarted until the transect was completed. After recovery to the ship the data were downloaded for analysis, and the sensors were recalibrated. Diffusive oxygen fluxes from the seawater into the sediments were calculated from the interfacial gradients, using a diffusion coefficient of 1.37×10^{-9} m^2 s^{-1} corrected for the porosity of 0.5 (Boudreau, 1996).

2.3. In situ temperature loggers

Loggers with 15 cm long Pt-100 temperature sensors were positioned in a transect (1, 1.4, 4 and 7 m from the vent) at the seafloor by the ROV (Suppl. Fig. 1). The loggers were preprogrammed to record the temperature with an interval of 7 s.

2.4. Sulfate reduction rates

Push cores were retrieved during the cruise with the ROV and 5 sediment cores were used for sulfate reduction rate (SRR) measurements, of which 3 in were taken of the vents and 2 approximately 30 m from the vents. Sediment subsamples were taken from the cores on the ship by cut-off 5 ml syringes, stoppered and stored anaerobically at 4 °C. The samples were placed in N_2 flushed zipper bags with a silicone tubing (15 cm long, 1 cm ID) filled with 1 M ascorbate adjusted to pH 11 as oxygen trap. Sulfate reduction rates were determined in the laboratory in Bremen within 3 weeks after sampling. To each cut-off syringe, tracer equivalent to 50 kBq $^{35}SO_4^{2-}$ was injected past the black rubber stopper. The tracer was equally distributed throughout the syringe. Incubation was stopped after >12 h by transferring the content of the syringe to 20 % (w/v) ZnAc and subsequent storage at −20 °C, until cold acidic Cr^{2+} distillation as described previously (Røy et al., 2014). Radioactivity was determined by scintillation counting.

2.5. Laboratory experiments

To better resolve the heterogeneity of the porewater chemistry around a CO_2 vent, experiments were performed in the laboratory. In an aquarium of 30 × 30 cm a 15 cm thick layer of North Sea sediment from the experimental site was deposited. In the center of the bottom was a nozzle through which gas was injected. Two perpendicular rows of each 4 pH sensors were mounted, so that the tips were at 8 cm depth in the sediment. One row consisted of electrodes (MI414, Microelectrodes Inc, Bedford USA) coupled to suitable mV amplifiers. The other row consisted of pH optodes (PHROB-PK7) coupled to a Firesting Pro amplifier (kindly provided by Pyroscience GmbH, Aachen, Germany). The two rows crossed at the gas vent. Initially a gentle stream of N_2 gas was vented to determine the position of the vent, then CO_2 gas was vented at a rate of 100 ml min^{-1} (7×10^{-5} mol s^{-1}). To avoid acidification *via* bottomwater, no water coverage was applied, thus the CO_2 vented into the atmosphere.

After the CO_2 gassing for 3 days, pH microprofiles were measured in a transect across the vent area, using electrodes from Microelectrodes Inc mentioned above. Subsequently, porewater was extracted using 10 cm long Rhizon samplers (Rhizosphere Research Products B.V., The Netherlands) along a transect at 0, 2, 4, 8 and 12 cm from the vent, at depths of 0, 4 and 8 cm. The samples were fixated with 50 μL saturated $HgCl_2$ for Total Alkalinity (TA) analyses or acidified with 100 μL suprapur HNO_3 for cation analyses. TA was determined by titration of 0.4−1 mL of sample using a mixture of methyl red and methylene blue as indicator and 0.0015 M HCl as titrant. Analyses were calibrated against International Association for the Physical Sciences of the Oceans (IAPSO) Seawater. The precision of the measurement was better than 1%. The cations Ca, Mg, K, Fe, Li, Mn, Si, B and Sr were measured by inductively coupled plasma optical emission spectrometry (ICP-OES, Thermo Scientific Icap 6500 duo) after diluting samples by a factor of 50 with 3% thermally distilled HNO_3. The ICP-OES was calibrated using 5 multi-element standard solutions prepared from single element ICP calibration standards. Measured concentrations of certified reference material for metals (CRM -SW, High-Purity Standards - seawater) were mainly within ±7 %.

2.6. Modeling

To simulate geochemical zonation and temperature effects of CO_2 venting during the *in situ* experiment, a sediment reaction-transport model was constructed using COMSOL 5.1 Multiphysics (COMSOL AB, Stockholm, Sweden). This program allows calculating mass and heat transport in a complex structure with a heterogeneous distribution of reactions and transport phenomena. A cylindrical sediment volume was modeled, of 6 m high and a radius of 10 m, radially symmetrical around a bubble stream in the center. The bubble stream was simplified to a gas channel in the sediment, a pipe with a source at 3 m below the sediment surface. At 3 m depth an inlet was assumed, as *in situ*, with a CO_2 concentration in equilibrium with seawater of 7 °C at 120 m depth. Using CO2Calc v4.0.9 (Robbins et al., 2010) this was calculated to be 408 mM.

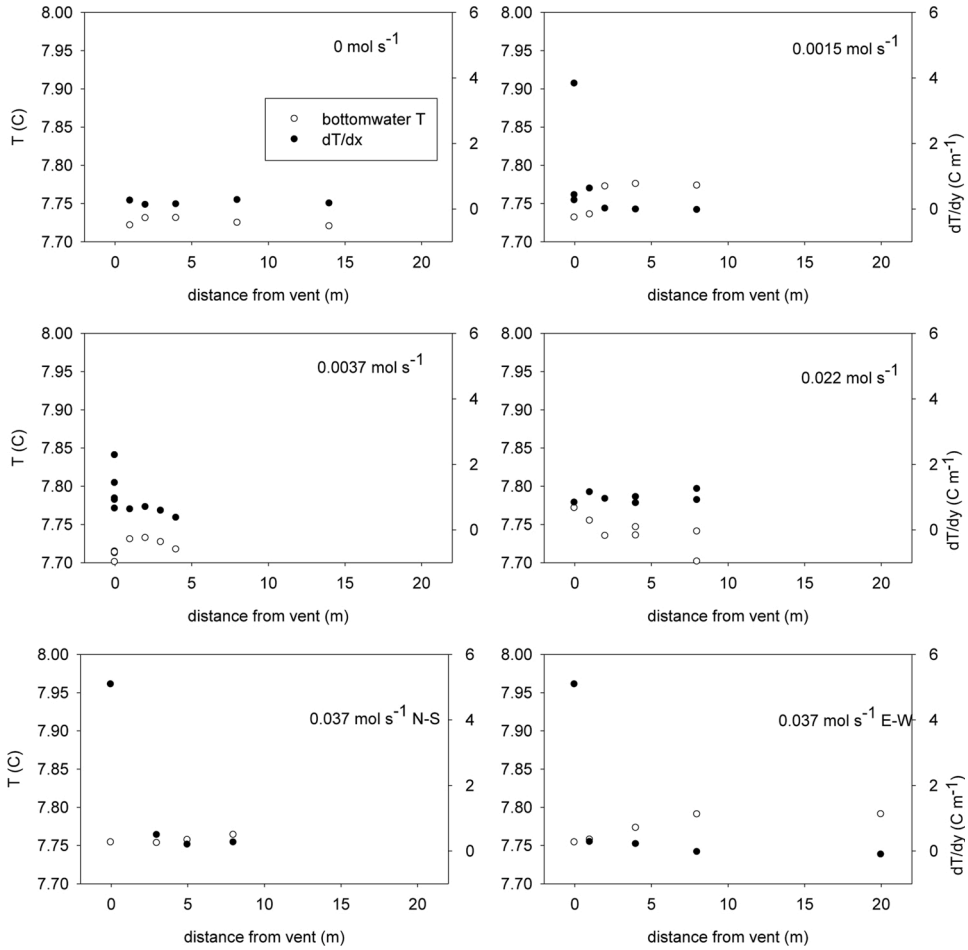

Fig. 2. Transects of the interfacial vertical temperature gradients dT/dy (solid circles, right axis) and the temperature of the bottom water (open circles, left axis). The effects inside the sediments, thus on the interfacial temperature gradients, are very local. There is no clear correlation between the temperature gradients in the vent and the CO_2 flux.

Suppl. Fig. 3 displays a 3D visualization of the modeled domain with an example of a modeled temperature distribution. The mesh-size was set 'physics controlled' and 'extremely fine'. The diameter of the gas channel was varied from 4, 8, 12–16 mm. The walls of the vent were assumed diffusionally permeable for CO_2 but not for DIC (further called H_2CO_3). This simulated a gas channel as CO_2 diffused out, but no solutes could diffuse in. The CO_2 levels at the channel wall were assumed in equilibrium with seawater and expressed as equilibrium concentrations. In the *in situ* experiment the mass flow was step-wise up-regulated from 0.0015, 0.0037, 0.022, to 0.037 mol s^{-1}. The resulting pressure changes and associated fingering resulted in several outlets (see Suppl. Fig. 4), thus per outlet the mass flow increased much less as the inflow (Strong, 2020). The changes in mass flow increased the number of main vents from 1, 3, 6–9 to 8, respectively, hence the mass flow in the simulations was assumed to be 0.0015, 0.0025 or 0.0047 mol s^{-1}. The increasing number of small intermittent vents was ignored. In the model, the mass flow in a vent, with a certain diameter, was modeled by adjusting the flow velocity in a vent. Transport and reactions were implemented by the module 'transport of diluted species'. Transport in the vent was assumed to be as in gas ($D = 1 \times 10^{-5}$ m^2 s^{-1}), transport in sediment was assumed diffusional for all species ($D = 1 \times 10^{-9}$ m^2 s^{-1}). Sediment permeability was determined in retrieved cores (diameter 36 mm, height 115 mm) using the falling head method (McCarthy and McCarthy, 1977). As the sediment permeability was found to be 3×10^{-13} (m^2) advection was not considered. As reactions were considered the dissolution of CO_2 in seawater (Eq. 1, 20 kJ mol^{-1}), the reaction of H_2CO_3 with calcite (10 kJ mol^{-1}):

$$CaCO_3 + CO_2\,(aq) + 2H_2O \rightarrow Ca^{2+} + 2HCO_3^- + H_2O \quad (2)$$

and of H_2CO_3 with silicate (73 kJ mol^{-1}):

$$MeSiO_3 + 2CO_2 + 4H_2O \text{ -> } MeSiO_3 + 2HCO_3^- + 2H_3O^+ \text{ -> } Me^{2+} + H_4SiO_4 + 2HCO_3^- + H_2O \quad (3)$$

where Me can be Ca or Mg. The enthalpies (Stumm and Morgan, 2012) were used to calculate the heat generation with the module 'heat transfer in solids', and coupled to the main multiphysics module. Reaction rates were estimated as follows: the calcite dissolution rate above pH 5 is 1×10^{-6} mol m^{-2} s^{-1} (Morse and Arvidson, 2002), as the average grain size was approximately 60 μm, the specific area is 1,200,000 (Mayer, 1994) m^2 m^{-3}, and assuming the sediment contained 2 % calcite (Stevenson et al., 1995) the rates were set to 2.4×10^{-2} s^{-1}. We assumed the reactivity with silicate as 1 % of the reactivity with calcite. In the end we extracted distributions of CO_2 in the gas channel, and H_2CO_3 and temperature distributions in the sediment.

The model aimed to approach observations in order of magnitude, namely the observed distribution of geochemical phenomena and the loss of CO_2. Further addition of complexities, such as including the full carbonate system and more convoluted geometries, led to instability of the program.

3. Results

The seafloor was flat, without ripples, consisting of fine sand mixed

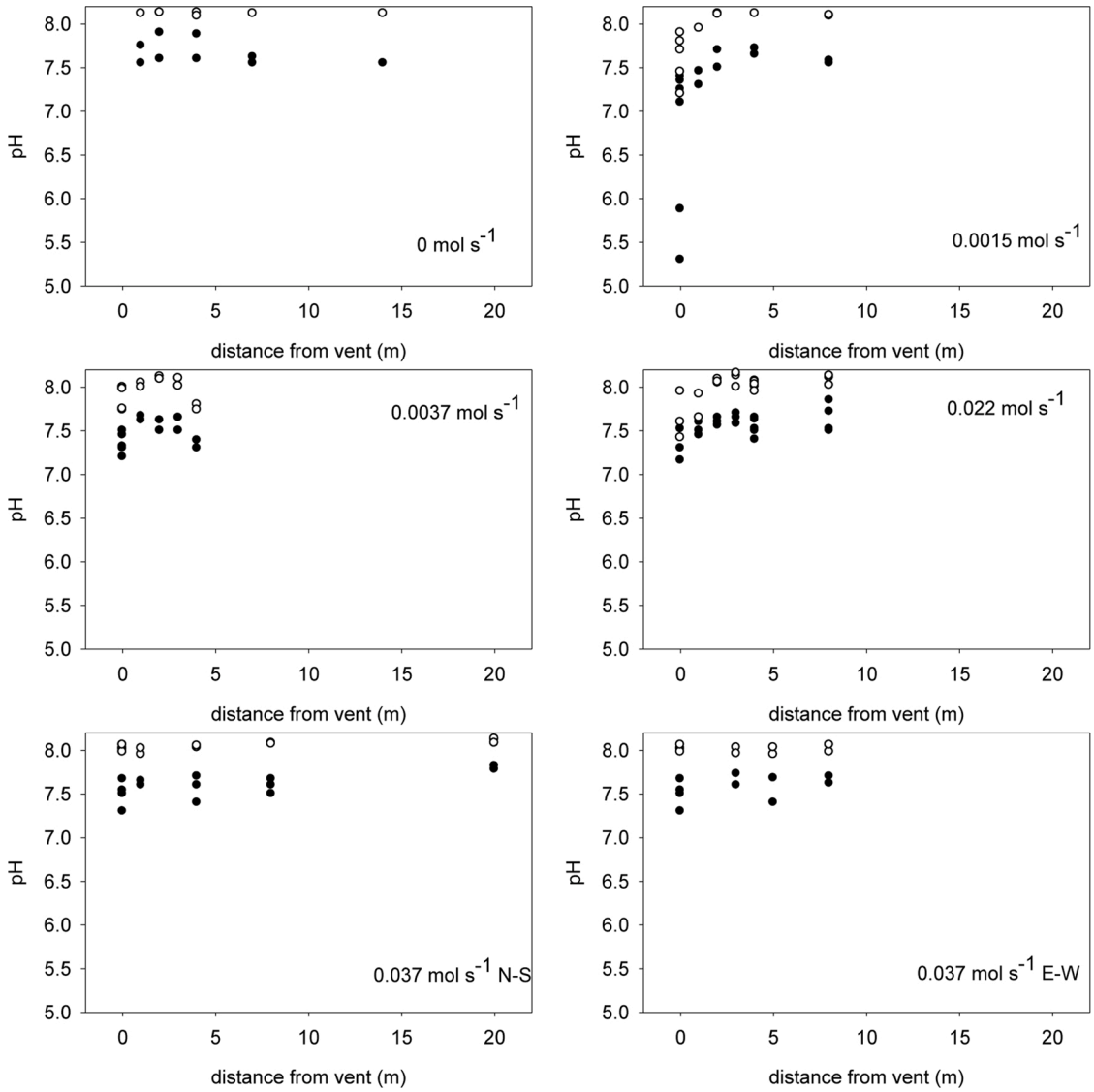

Fig. 3. Transects of the pH values at 0.06 m bsf (solid circles) and the pH values at the sediment surface (open circles).

with silt. There were few signs of burrowing fauna. Before the *in situ* experiment started no gas bubbles escaping the sediment were observed. Within 15 min after switching on the CO_2 venting, bubbles were observed.

The *in situ* profiles showed a clear effect of CO_2 venting on the sediment chemistry (Fig. 1). Background profiles (Fig. 1A, B), not influenced by CO_2 venting, showed an oxygen penetration depth of approximately 0.01 m, no temperature changes and a gradual pH decrease with depth to a value of 7.5. Free sulfide was present, but below the detection limit (1 μM). The oxygen reduction potential (ORP) decreased to −300 mV at 0.06 m below seafloor (bsf). Little or no variation was observed between profiles from different sites. Venting could drastically change the profiles, however, only very close to or inside the actual vents. In the transects we found background profiles until the profiler approached the vents to less than 1 m distance. When placed on top of a vent the profiles often became irregular (Fig. 1C, D). In the vents the pH decreased drastically, occasionally down to 5. Oxygen profiles measured by different microsensors on the same vent could show a penetration depth that was decreased or increased as compared to the background (Fig. 1C). The oxygen-redox potential became irregular but did not decrease further, but rather increased. Remarkably, the temperature inside the vents often increased with depth (Fig. 1D, 2). Also the temperature loggers placed at 15 cm depth near the vent recorded temperature increases upon start of the CO_2 venting (Suppl. Fig. 2).

The effect of venting on the sediment temperature, summarized in Fig. 2, was not proportional to the venting rate. The temperature gradients were up to 5 °C m^{-1}, but highly variable (Suppl. Fig. 6). For example, no temperature effects were observed at a venting rate of 0.022 mol s^{-1}. Multiple measurements at the venting site resulted in either steep gradients or virtual absence of gradients (Fig. 2, 0.0015 and 0.022 mol s^{-1}). Enhanced temperatures were never measured further than 1 m from the vents. These observations point to very local effects of venting on the temperature gradients: only when the sensor enters exactly the venting channel an effect is measured. Such a positioning is a matter of chance. The bottom water temperature is not influenced by the venting. Increases in temperature were also observed in loggers positioned at 15 cm depth near the CO_2 injection point during the whole experiment (Flohr et al., 2020). (Supp. Fig. 1).

The pH values in the sediments and bottom water were also only locally influenced by the CO_2 venting (Fig. 3). The bottom water pH was decreased by the venting. Similar as with temperature, also no pH effect in sediments was observed beyond 1 m from the vent site. The pH decrease in the vent area was not proportional to the venting rate. For

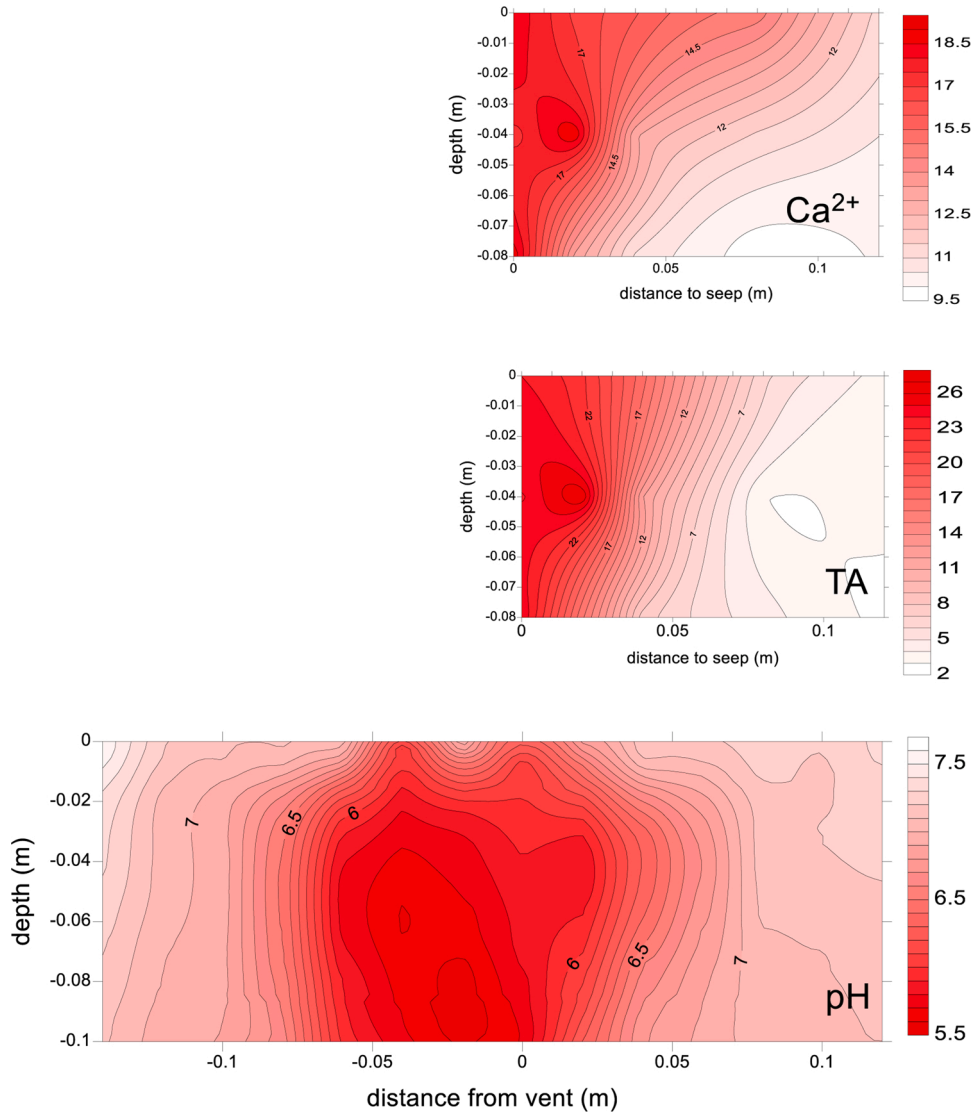

Fig. 4. Contour plots of pH, Ca and TA. The vent has a branched structure. The distribution of Ca and TA follows that of the pH. Numbers on the scale for Ca and TA are in mol m^{-3}.

example pH values below 7 were observed when CO_2 venting was 0.0015 mol s^{-1}, while no effects were observed in the vent site when 0.037 mol s^{-1} was vented. This again points to a very small area that is influenced by the venting: effects are only visible when the microsensors enter exactly in the venting channel.

To better resolve the heterogeneity of the porewater chemistry around a CO_2 vent, vent experiments were performed in the laboratory. Initially N_2 was vented gently in the sediment tank. Two hours after mounting the pH sensors at 0.08 m depth, the gas flow was switched from N_2 to CO_2. Subsequently, a pattern of pH dynamics developed. The pH in and near (0 and 0.02 m distance) the gas vent decreased within hours to a value of 6, while the pH values at 0.04 and 0.08 m distance remained stable at pH 7.1. The pH pattern showed a slightly wobbly vent channeling. During the CO_2 bubbling, the outlet at the surface did move occasionally between locations about 5 cm apart. After 3 days the experiment was continued by detailed pH profiling along a transect across the vent, followed by porewater sampling. The pH profiles were combined into a contourplot (Fig. 4) showing that the pH decrease occurred in a plume surrounding the vent channel at position 0. To the right of the original vent center (position 0), the pH effect is visible to about 0.05 m distance. To the left the vent seemed to branch more and pH effects were visible to 0.1 m distance. The pH distribution at 7 cm depth showed that the pH effect of the vent reached about 7 or 8 cm from the vent channel.

The pattern of Ca^{2+} and TA resembled the pH, with strongly enhanced concentrations in the vent channel. Sr^{2+} had exactly the same distribution as Ca^{2+}, while the other cations (Si, Fe, Mg, Mn, K, Li, B) did not have a structured distribution (not shown).

The benthic degradation rates of organic matter were assessed from aerobic respiration rates and sulfate reduction rates. Oxygen uptake rates, calculated from microsensor profiles, were not significantly affected by increased CO_2 venting. The rates in the venting area were slightly lower than those in the background area, but venting significantly decreased the sulfate reduction rates to about half (Fig. 5). The areal rates for O_2 uptake ranged between 3.5–5.5 $\times$ 10^{-8} mol m^{-2} s^{-1}. SRR, integrated over the upper 0.16 m, decreased from 1.6 $\times$ 10^{-8} mol m^{-2} s^{-1} to 0.8 $\times$ 10^{-8} mol m^{-2} s^{-1} at the end of the venting experiment. The SO_4^{2-} concentration was 28 mM at all depths. Hence, degradation in the sediments is dominated by aerobic processing, even more so upon CO_2 venting.

3.1. Reaction-transport model

As expected, the model calculated a loss of CO_2 along the gas channel

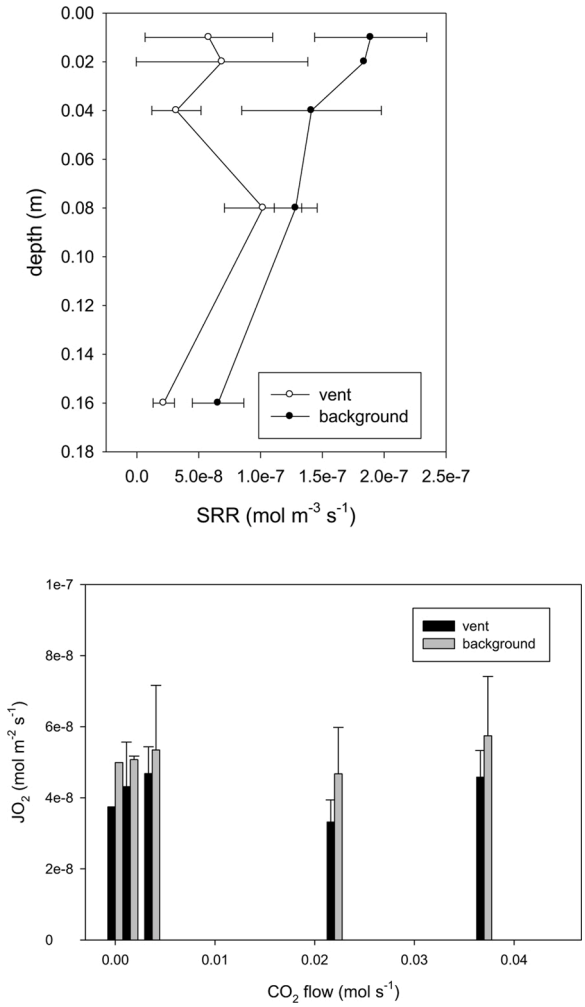

Fig. 5. Activity data show that vents have lower SRR than background sediments (left panel) but similar oxygen uptake rates (right panel).

resulting in a gradual decrease of CO_2 at the channel wall from the point of injection to the sediment surface (Fig. 6).

The mass loss from the gas channel was sensitive to the assumed diameter of the channel (Fig. 7), with strongly increasing mass loss with larger channel diameter. The mass loss was less sensitive to the mass flow, although with increasing mass flow a lower fraction of the CO_2 was lost. By varying the diameter of the channel and the mass flow in a reasonable range the losses could vary from 10 to 90 %. As the measured losses were between 25 and 75 % (Flohr et al., 2020; Schaap et al., 2020), the modeled fits suggest gas channels to have functional radii of 4–6 mm.

The lost CO_2 was laterally transported into the sediment, where it dissolves in the porewater to H_2CO_3, that reacts with the sediment matrix. This results in heat development, and in a temperature distribution pattern that resembles the shape of a flame (Suppl. Fig. 3). As all H_2CO_3 reacts, the temperature increase is proportional to the CO_2 loss from the gas channel. Temperature increase could be up to several tens of degrees close to the injection point, but near the sediment surface the temperature effects were much less (Fig. 8).

From the modeled data also the vertical temperature gradients at the sediment surface were extracted, to allow comparison with the temperature gradients measured with the *in situ* profiler. Fig. 9 demonstrates how local temperature effects are at the sediment surface. Beyond 10 cm from the vent the vertical temperature gradients are less than 10 % of the maximum in the channel. The highest measured temperature gradient (Fig. 2) was 5 °C m^{-1}, much lower than model outcomes (Fig. 9).

4. Discussion

The *in situ* profiles indicated that the effects of CO_2 leakage on sediment geochemistry are limited to the direct vicinity of the vent. The effects of venting were never visible beyond 1 m distance from the vent, but the true heterogeneity is of a much smaller scale. The 3 pH sensors that were mounted 3–4 cm apart on the profiler consistently showed different pH profiles, when the profiler was positioned above a CO_2 vent (Suppl. Fig. 5). The vent opening is only a few cm in diameter, and the data indicate that only the channel itself and possibly its direct surrounding is influenced by the CO_2 bubbles. The profiles did not show a consistent correlation between pH decrease and CO_2 venting rates. For example, the pH decrease measured at a venting rate of 0.0015 mol s^{-1} was much stronger than at a venting rate of 0.037 mol s^{-1}. Because the venting opening was only a few cm in diameter it was a matter of chance if the opening was penetrated by the microsensor. Thus the vent channels are narrow and the effects of CO_2 venting are confined to the bubble channels and its direct surroundings.

This was confirmed by the laboratory experiments where the zone of reduced pH could be accurately documented. These measurements confirmed that the channel is indeed narrow, and that the affected zone is limited to a few cm away from the channel. As the gas bubbles irregularly changed the course of the channel slightly, near the sediment surface a larger area than around a single channel was acidified and a branching structure was observed in the pH distribution (Fig. 5). Below the branching, at 8 cm depth a narrow zone of pH decrease is observed.

The size and shape of the plume inside the sediment has large consequences for the buffering and CO_2 absorption capacity of sediment on the CO_2. The limited size of the low-pH zone is not only due to the relatively short time of the experiments, but can be understood from mass transfer phenomena. Assuming diffusion controls transport from the channel into the surrounding medium and the geometry of the system approximates an infinitely long cylinder in an infinite medium, we can define a mass boundary layer surrounding the cylinder where the CO_2 concentration and its associated chemistry gradually decrease from the surface level (S_i) towards the level at infinite distance (S_b). The transport from the surface is controlled by the effective boundary layer (Lewis and Whitman, 1924), a linear profile of hypothetical thickness (δ_h). The size of δ_h is found by intersecting the tangent of the substrate profile at the cylinder surface and S_b. The thickness of δ_h depends on the diameter of the cylinder (d), the diffusion coefficient (D), the perpendicular liquid velocity (u), the liquid density (ρ) and the liquid viscosity (μ), as can be seen from the empirical relation for the Sherwood number for a vertical cylinder in an infinite medium:

$$Sh = 0.3 + \frac{0.62 Re^{\frac{1}{2}} Sc^{\frac{1}{3}}}{\left(1 + \left(\frac{0.4}{Sc}\right)^{\frac{2}{3}}\right)^{\frac{1}{4}}} \left(1 + \left(\frac{Re}{282000}\right)^{\frac{5}{8}}\right)^{\frac{4}{5}} = \frac{kd}{D} \quad (4)$$

where Re is the Reynolds number, Sc the Schmidt number and k the mass transfer coefficient:

$$Re = \frac{u\rho d}{\mu} \text{ and } Sc = \frac{\mu}{\rho D}$$

Eq. 4 is derived from an equation describing the heat transfer from a cylinder (Churchill and Bernstein, 1977). Heat transfer follows the same physical rules as diffusion, as both are driven by random motion of molecules (Welty et al., 2014), and the Prandtl number Pr can be replaced by Sc and the Nusselt number Nu by Sh to obtain the relation for mass transfer.

The mass transfer coefficient k is proportional to the diffusion coefficient D and the thickness of δ_h, so:

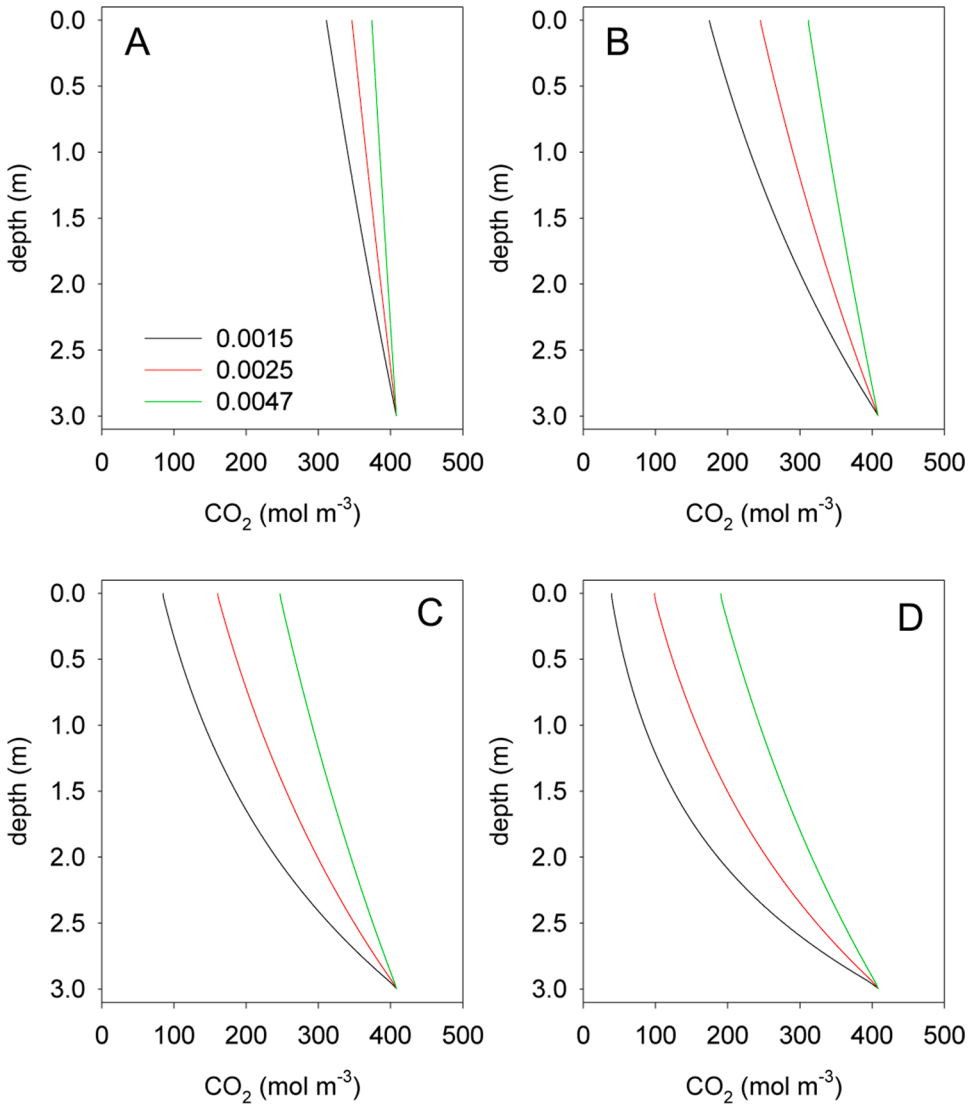

Fig. 6. Modeled concentration profiles in the gas channel expressed as equilibrium concentrations with seawater, with the inlet at 3 m bsf and the outlet at the surface (depth = 0). The numbers in the legend are the mass flow rates in mol s^{-1}. The plots in panels A-D are modeled with radii of the gas channel 0.002, 0.004, 0.006 and 0.008 m, respectively.

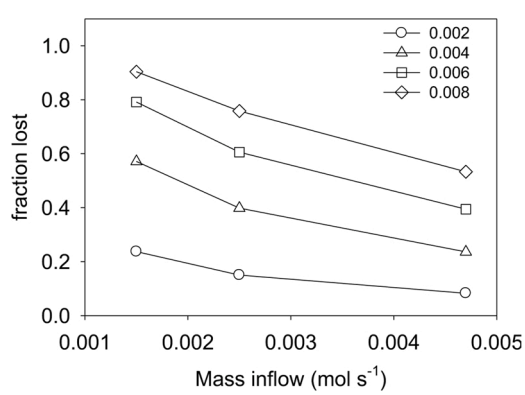

Fig. 7. The calculated mass loss as fraction of the injected mass flow. Different symbols represent different channel radii (in m). As the volume of the gas channel was assumed to remain constant with depth, the concentration in the channel reflects the lateral loss of CO_2. The measured losses were between 25 and 75 %, depending on the method used.

$$k = \frac{D}{\delta_h} \text{ and } J = k(S_i - S_b) = D\frac{S_i - S_b}{\delta_h} \tag{5}$$

In absence of flow Re = 0 and hence according to Eq. 4 Sh = 0.3.

$$\text{As } Sh = \frac{kd}{D} \text{ and } k = \frac{D}{\delta_h},\ \delta_h = \frac{d}{Sh} = 3d \tag{6}$$

Eq. 6 means that the effective mass boundary layer for heat and solutes around a cylinder in a stagnant medium is finite and 3 times its diameter. Eq. 6 reflects the maximum estimate for the effective thickness of the mass boundary layer around a vent channel, advection will make the zone smaller. This is counterintuitive as one might consider that transport spreads chemistry, however it also dilutes the vent chemistry and its effects. Thus the size of the influenced zone is a matter of geometry only: the constant source results in a mass flux that with increasing distance to the source goes through an exponentially larger area (as $A=\pi r^2$, with A the area per m length and r the distance to the center of the source). Hence the areal flux is exponentially decreasing with distance, as the gradient asymptotically approaches 0. Reactions in the medium around the cylinder that consume the diffusing substance will further reduce the zone influenced by substrates leaking from the cylinder. As most protons are coupled to buffering agents, for pH effects

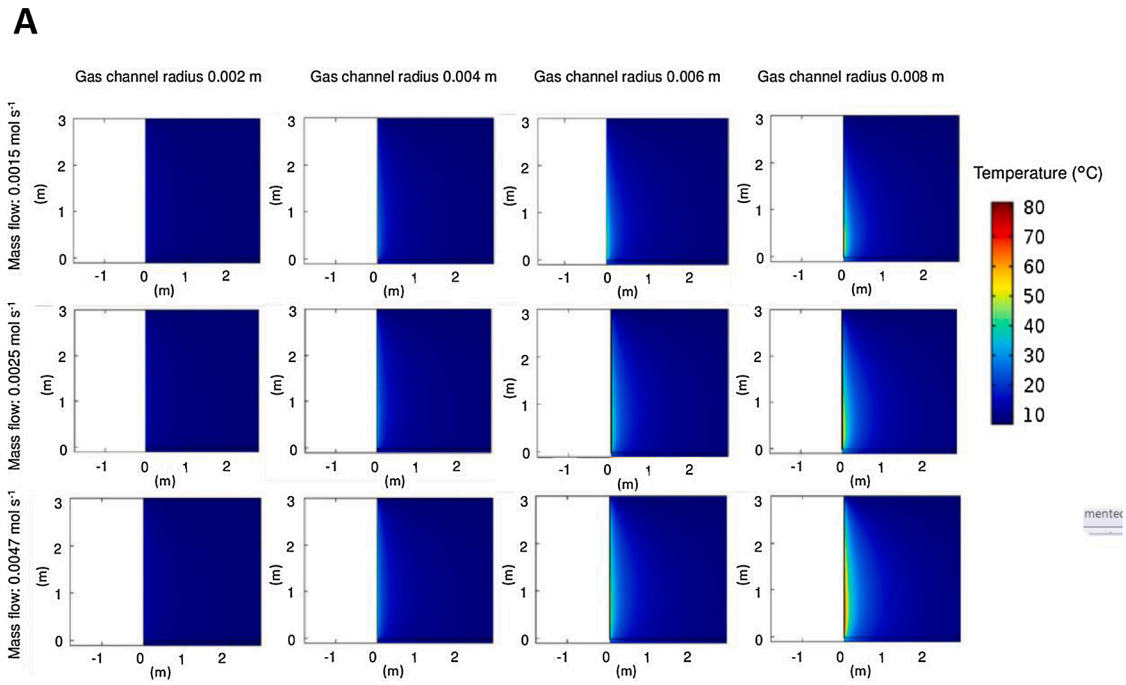

Fig. 8. Modeled T profiles with mass flows of 0.0015, 0.0025 or 0.0047 mol s^{-1}, into gas channels with radii of 0.002-0.008 m.

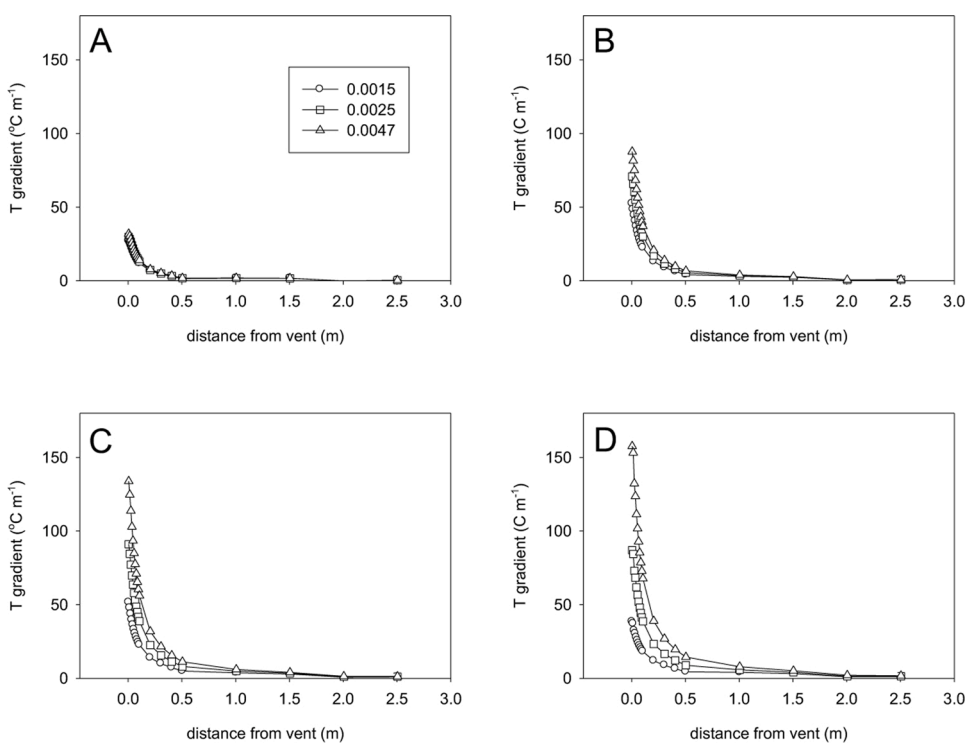

Fig. 9. Modeled T gradients at the sediment surface show that effects of CO_2 venting on T attenuates quickly with distance. Modeled were mass flows of 0.0015, 0.0025 or 0.0047 mol s^{-1}, into gas channels with radii of 0.002, 0.004, 0.006 and 0.008 m (A-D, resp.).

we should also consider the transport of buffering solutes, in seawater mainly the carbonate system. The proton-buffering solutes will diffuse from an infinite volume towards the cylindrical source through an area that is exponentially decreasing in size with distance to the CO_2 source, hence the buffering flux is exponentially increasing when nearing the source. The lateral transport around the bubble channel will lead to loss of CO_2 from the gas stream and enrichment of N_2, due to diffusion from the porewater into the bubbles. Buffering reactions (Eqs. 2 and 3) will increase the pH and increase the dissolution of CO_2, and increasing the loss of CO_2 from the channel. These dissolution reactions will also be controlled by lateral diffusion of their reaction products (cations and bicarbonate) away from the channel zone, because solubility saturation of the different minerals may be approached in the narrow reaction zone.

A limitation of this approach is that the real gas channel is not of infinite length, and that our measurements are near the end of the pipe.

Therefore, we also modeled the pipe with COMSOL, where events in a well described structure of finite dimensions is calculated. Our COMSOL model was kept very simple. It was not used to calculate the carbonate system including the pH profiles, and we assumed that the calcite and silicates were not depleted, which indeed did not occur during the experiment (Lichtschlag et al., 2020). We assumed a strongly simplified structure, a pipe carrying the injected gas in a straight line to the surface. The separate gas bubbles and branching were ignored and the carbonate system was simplified to CO_2 and H_2CO_3, that could react with the sediment, generating heat. As we aimed for order of magnitude precision we did not model the transport and reactions of all inorganic carbonate species and assumed that the diffusion coefficient of all carbonate species was 10^{-9} m^2 s^{-1}. In reality, vents are a 3 phase system with gas bubbles, porewater and sediment, that may form a complex branching structure, with unknown curvature and even gas chambers (Haeckel et al., 2007). Yet, the model does approximate observations, as the results showed the local aspect of the geochemical phenomena, and within order of magnitude the loss of CO_2 and the heat generation in the surrounding sediments. The loss of CO_2 from the channel is stoichiometrically coupled to the generation of heat, and, according to the model, this resulted in remarkably strong temperature increases. Indeed, elevated temperatures were observed upon CO_2 venting (Figs. 1, 2 and Suppl. Figs. 2, 5, 6). However, the modeled steady state temperature gradients near the sediment surface are larger than those observed (Suppl. Fig. 6). Partially, this is because the experiment was for practical reasons not continued until steady state, which would have taken years (Haeckel et al., 2007). Secondly, the difference between model outcome and measurements near the sediment surface can be attributed to an exchange phenomenon (Stöhr et al., 2004), where it was documented by dye experiments that when a bubble leaves the sediment an equal volume of bottom water is sucked into the sediment. Thus a series of bubbles in the channel result in a pulsating vertical motion of the porewaters, enhancing dispersion. This phenomenon will reduce the temperature effects near the surface, and attenuate the geochemical effects of CO_2. This mixing by bubbles explains the observed low total alkalinity in the upper 10 cm of the CO_2 vent as documented elsewhere (Lichtschlag et al., 2020). The phenomenon was coined 'bubble-induced irrigation' (Haeckel et al., 2007) and it was calculated that eventually, after several years, the whole channel of 3 m long will be influenced by the chemistry of the bottomwater (Haeckel et al., 2007).

According to our model, the diameter of the channel strongly influences the fraction of the CO_2 that is laterally lost. The best fit was for a gas channel with a radius of 4–6 mm, a diameter of the gas channel that must be seen as a functional size, and could well be larger than the actual size of the bubbles (Haeckel et al., 2007).

The extent of pH decrease that was measured is less than can be expected from calculations. Using the program CO2calc (Robbins et al., 2010) it can be calculated that bubbling seawater (alkalinity 2.3 mol m^{-3}) with pure CO_2 at 20 °C and 1 atm will, in equilibrium, reduce the pH to 4.9. In the *in situ* experiment at 120 m depth, bubbling pure CO_2 should lead to a pH decrease to 3. The observed lowest values were always higher, namely pH 6 in the laboratory and pH 5 *in situ*. This discrepancy is explained by dilution by bottomwater and reactions of H_2CO_3 with the sediment. The bubble-induced irrigation, as detailed above, will mix the acidic porewater with bottomwater of a higher pH. The H_2CO_3 will react with the sediment *via* the two processes in Eqs. 2 and 3 that consume CO_2 and acidity. The corrosion of carbonates (Eq 2) is much faster than that of silicate (Eq. 3) (Wallmann et al., 2008). Indeed, in the laboratory experiment no elevated Si was found in the porewater, while Ca^{2+} levels were strongly enhanced. The pH buffering by sediment will decrease the effects of CO_2 on porewater chemistry to a zone close to the bubble tube. Obviously, eventually the $CaCO_3$ pools in the venting channels will be depleted (Fink et al., 2017). Then the pH will decrease further and silicate weathering may become the mayor buffering process.

The effect of venting on biogeochemistry was small. The aerobic respiration rates in the vent area were the same as in the background, while sulfate reduction is reduced only in the very vent channel. Thus effects of CO_2 venting on the element cycling in the local ecosystem cannot be expected.

The generation of heat should be considered in future modeling of natural or artificial vents. The heat generation is significant, and can lead to very high local temperatures, certainly upon high pressure injection for CCS in wells of several km deep. The increased temperature will reduce viscosity of the porewater, enhancing convection and reactivity with sediments. Importantly, the process rates between the carbonate system and silicates (Eqs. 2 and 3) drastically increase with temperature (Brady and Carroll, 1994).

The results that sediments do not get saturated by the injected compounds is counterintuitive. A study with the pH Eddy Covariance method, which combines measured DIC fluxes with equilibrium estimates and a plume model, found that less than 15 % of the injected CO_2 was lost(Koopmans et al., 2020). However, in two other accompanying studies it was found that 25–75% of the CO_2 that is injected into the sediment at 3 m bsf does not reach the water column (Flohr et al., 2020; Schaap et al., 2020). Our data, corroborated by a model, show that such losses are well explained by the sum of lateral diffusion into the sediment and reactions with the sediment. As the storage of CO_2 is planned to be at several km depth, it is seems likely that most of possibly escaping CO_2 cannot reach the watercolumn.

In summary, upon leaving the injector CO_2 is transferred upwards to the sediment surface in a narrow channel. During this transport CO_2 partially dissolves and diffuses laterally in the sediments where it engages in a series of reactions with the sediment that generates heat and dissipates protons. Also most of the generated heat will dissipate laterally. The effects will be limited to a narrow zone around the gas channel. No effects on the local ecology can be expected.

CRediT authorship contribution statement

Dirk de Beer: Conceptualization, Data curation, Formal analysis, Investigation, Methodology, Software, Visualization, Writing - original draft, Writing - review & editing. **Anna Lichtschlag:** Methodology, Data curation, Writing - review & editing. **Anita Flohr:** Methodology, Writing - review & editing. **Marit Rianne van Erk:** Methodology, Writing - review & editing. **Soeren Ahmerkamp:** Software. **Moritz Holtappels:** Methodology. **Matthias Haeckel:** Writing - review & editing. **James Strong:** Writing - review & editing.

Declaration of Competing Interest

The authors declare that they have no known competing financial interests or personal relationships that could have appeared to influence the work reported in this paper.

Acknowledgements

We thank the crew of the RSS James Cook for the perfect support during the cruise. We thank Carla Sands and Doug Connelly for the constructive coordination. We are thankful for discussions with and help from Tim Ferdelman. This project has received funding from the European Union's Horizon 2020 research and innovation program under grant agreement No. 654462 STEMM-CCS.

Appendix A. Supplementary data

Supplementary material related to this article can be found, in the online version, at doi:https://doi.org/10.1016/j.ijggc.2020.103244.

References

Boudreau, B.P., 1996. The diffusive tortuosity of fine-grained unlithified sediments. Geochim. Cosmochim. Acta 60, 3139–3142.

Brady, P.V., Carroll, S.A., 1994. Direct effects of CO2 and temperature on silicate weathering: possible implications for climate control. Geochim. Cosmochim. Acta 58, 1853–1856.

Churchill, S.W., Bernstein, M., 1977. A correlating equation for forced convection from gases and liquids to a circular cylinder in Crossflow. J. Heat Transfer 99, 300–306.

de Beer, D., Haeckel, M., Neumann, J., Wegener, G., Inagaki, F., Boetius, A., 2013. Saturated CO_2 inhibits microbial processes in CO_2-vented deep-sea sediments. Biogeosciences 10, 5639–5649.

Dean, M., Blackford, J., Connelly, D., Hines, R., 2020. Insights and guidance for offshore CO2 storage monitoring based on the QICS, ETI MMV, and STEMM-CCS projects. Int. J. Greenh. Gas Control. 100, 103120.

Fabricius, K.E., Langdon, C., Uthicke, S., Humphrey, C., Noonan, S., De'ath, G., Okazaki, R., Muehllehner, N., Glas, M.S., Lough, J.M., 2011. Losers and winners in coral reefs acclimatized to elevated carbon dioxide concentrations. Nat. Clim. Chang. 1, 165–169.

Fink, A., den Haan, J., Chennu, A., Uthicke, S., de Beer, D., 2017. Ocean acidification changes abiotic processes but not biotic processes in coral reef sediments. Front. Mar. Sci. 4.

Flohr, A., Gros, J., Matter, J.M., James, R.H., Strong, J., Saw, K., Brown, R., Flude, S., Day, C., Kate Peel, K., Pearce, C., Connelly, D., 2020. Quantification of leakage from sub-seabed CO_2 storage using natural and added geo-chemical tracers. Int. J. Greenh. Gas Control (this issue).

Glud, R.N., Wenzhöfer, F., Middelboe, M., Oguri, K., Turnewitsch, R., Canfield, D., Kitazato, H., 2013. High rates of benthic microbial activity at 10.900 meters depth: results from the Challenger Deep (Mariana trench). Nat. Geosci. 6, 284–288.

Guilini, K., Weber, M., de Beer, D., Schneider, M., Molari, M., Lott, C., Bodnar, W., Mascart, T., De Troch, M., Vanreusel, A., 2017. Response of Posidonia oceanica seagrass and its epibiont communities to ocean acidification. PLoS One 12, e0181531.

Haeckel, M., Boudreau, B.P., Wallmann, K., 2007. Bubble-induced porewater mixing: a 3-D model for deep porewater irrigation. Geochim. Cosmochim. Acta 71, 5135–5154.

Hall-Spencer, J.M., Rodolfo-Metalpa, R., Martin, S., Ransome, E., Fine, M., Turner, S.M., Rowley, S.J., Tedesco, D., Buia, M.C., 2008. Volcanic carbon dioxide vents reveal ecosystem effects of ocean acidification. Nature 454, 96–99.

Hofmann, L.C., Fink, A., Bischof, K., de Beer, D., 2015. Microsensor studies on Padina from a natural CO2 seep: implications of morphology on acclimation to low pH. J. Phycol. 51, 1106–1115.

Konno, U., Tsunogai, U., Nakagawa, F., Nakaseama, M., Ishibashi, J., Nunoura, T., Nakamura, K., 2006. Liquid CO_2 venting on the seafloor: yonaguni Knoll IV hydrothermal system, Okinawa Trough. Geophys. Res. Lett. 33, L16607.

Koopmans, D., Meyer, V., Holtappels, M., Schaap, A., Deward, M., Färber, P., Long, M., Connelly, D., de Beer, D., 2020. Chemical detection of a controlled release of carbon dioxide gas at the seafloor using pH eddy covariance. Int. J. Greenh. Gas Control (this issue).

Lewis, W.K., Whitman, W.G., 1924. Principles of gas absorption. Ind. Eng. Chem. 16, 1215–1220.

Lichtschlag, A., James, R.H., Stahl, H., Connelly, D., 2015. Effect of a controlled sub-seabed release of CO2 on the biogeochemistry of shallow marine sediments, their pore waters, and the overlying water column. Int. J. Greenh. Gas Control 38, 80–92.

Lichtschlag, A., Olierook, D., Peel, K., Haeckel, M., Flohr, A., Marieni, C., James, R., Pearce, C., Connelly, D., 2020. Impact of CO_2 leakage from sub-seabed carbon dioxide capture and storage on sediment geochemistry. Int. J. Greenh. Gas Control (this issue).

Long, M.H., Charette, M.A., Martin, W.R., McCorkle, D.C., 2015. Oxygen metabolism and pH in coastal ecosystems: eddy Covariance Hydrogen ion and Oxygen Exchange System (ECHOES). Limnol. Oceanogr. Methods 13, 438–450.

Mayer, L.M., 1994. Surface area control of organic carbon accumulation in continental shelf sediments. Geochim. Cosmochim. Acta 58, 1271–1284.

McCarthy, D.F., McCarthy, D.F., 1977. Essentials of Soil Mechanics and Foundations. Reston Publishing Company Virginia.

Mevenkamp, L., Ong, E.Z., Van Colen, C., Vanreusel, A., Guilini, K., 2018. Combined, short-term exposure to reduced seawater pH and elevated temperature induces community shifts in an intertidal meiobenthic assemblage. Mar. Environ. Res. 133, 32–44.

Molari, M., Guilini, K., Lott, C., Weber, M., de Beer, D., Meyer, S., Ramette, A., Wegener, G., Wenzhöfer, F., Martin, D., Cibic, T., De Vittor, C., Vanreusel, A., Boetius, A., 2018. CO_2 leakage alters biogeochemical and ecological functions of submarine sands. Sci. Adv. 4.

Morse, J.W., Arvidson, R.S., 2002. The dissolution kinetics of major sedimentary carbonate minerals. Earth. Rev. 58, 51–84.

Rizzo, A.L., Caracausi, A., Chavagnac, V., Nomikou, P., Polymenakou, P.N., Mandalakis, M., Kotoulas, G., Magoulas, A., Castillo, A., Lampridou, D., Marusczak, N., Sonke, J.E., 2019. Geochemistry of CO_2-Rich gases venting from submarine volcanism: the case of Kolumbo (Hellenic volcanic arc, Greece). Front. Earth Sci. 7.

Robbins, L.L., Hansen, M.E., Kleypas, J.A., Meylan, S.C., 2010. CO2calc: A User-Friendly Seawater Carbon Calculator for Windows, Mac OS X, and iOS (iPhone), Open-File Report. Reston, VA.

Røy, H., Weber, H.S., Tarpgaard, I.H., Ferdelman, T.G., Jørgensen, B.B., 2014. Determination of dissimilatory sulfate reduction rates in marine sediment via radioactive ^{35}S tracer. Limnol. Oceanogr. Methods 12, 196–211.

Russell, B.D., Connell, S.D., Uthicke, S., Muehllehner, N., Fabricius, K.E., Hall-Spencer, J. M., 2013. Future seagrass beds: Can increased productivity lead to increased carbon storage? Mar. Pollut. Bull. 73, 463–469.

Schaap, A., Koopmans, D., Holtappels, M., Dewar, M., Arundell, M., Papadimitriou, S., Hanz, R., Monk, S., Mowlem, M., Loucaides, S., 2020. Quantification of a subsea CO_2 release with lab-on-chip sensors measuring benthic gradients. Int. J. Greenh. Gas Control. (this issue).

Stevenson, A.G., Tait, B.A.R., Richardson, A.E., Smith, D.T., Nicholson, R.A., Stewart, H. R., 1995. In: The Geochemistry of Sea-Bed Sediments of the United Kingdom Continental Shelf; the North Sea, the Hebrides and West Shetland Shelves, and the Malin-Hebrides Sea Area. British Geological Survey Technical Report WB/95/28C. British Geological Survey, Edinburg.

Stöhr, M., Goharzadeh, A., Khalili, A., 2004. Investigation of flow and transport in the vicinity of uprising bubbles near the interface of permeable sediments using 3D PLIF and PIV. In: 12th International Symposium on Applications of Laser Techniques to Fluid Mechanics. Lisbon, pp. 1–11.

Strong, J., et al., 2020. Map of vent site. Int. J. Greenh. Gas Control (this issue).

Stumm, W., Morgan, J.J., 2012. Aquatic Chemistry: Chemical Equilibria and Rates in Natural Waters, 3 ed. Wiley.

Vielstädte, L., Linke, P., Schmidt, M., Sommer, S., Haeckel, M., Braack, M., Wallmann, K., 2019. Footprint and detectability of a well leaking CO_2 in the Central North Sea: Implications from a field experiment and numerical modelling. Int. J. Greenh. Gas Control. 84, 190–203.

von Deimling, J.S., Greinert, J., Chapman, N.R., Rabbel, W., Linke, P., 2010. Acoustic imaging of natural gas seepage in the North Sea: sensing bubbles controlled by variable currents. Limnol. Oceanogr. Methods 8, 155–171.

Wallmann, K., Aloisi, G., Haeckel, M., Tishchenko, P., Pavlova, G., Greinert, J., 2008. Silicate weathering in anoxic marine sediments. Geochim. Cosmochim. Acta 72, 2895–2918.

Wan, S., Clift, P.D., Zhao, D., Hovius, N., Munhoven, G., France-Lanord, C., Wang, Y., Xiong, Z., Huang, J., Yu, Z., Zhang, J., Ma, W., Zhang, G., Li, A., Li, T., 2017. Enhanced silicate weathering of tropical shelf sediments exposed during glacial lowstands: a sink for atmospheric CO_2. Geochim. Cosmochim. Acta 200, 123–144.

Welty, J., Rorrer, G.L., Foster, D.G., 2014. Fundamentals of Momentum, Heat, and Mass Transfer, 6th ed. Wiley and sons.

Ziogou, F., Gemeni, V., Koukouzas, N., de Angelis, D., Libertini, S., Beaubien, S.E., Lombardi, S., West, J.M., Jones, D.G., Coombs, P., Barlow, T.S., Gwosdz, S., Krüger, M., 2013. Potential environmental impacts of CO_2 leakage from the study of natural analogue sites in Europe. Energy Procedia 37, 3521–3528.